

Blood–Brain Barrier Remodeling in an Organ-on-a-Chip Device Showing Dkk1 to be a Regulator of Early Metastasis

Trisha M. Westerhof, Benjamin A. Yang, Nathan M. Merrill, Joel A. Yates, Megan Altemus, Liam Russell, Anna J. Miller, Liwei Bao, Zhifen Wu, Peter J. Ulintz, Carlos A. Aguilar, Aki Morikawa, Maria G. Castro, Sofia D. Merajver, and Christopher R. Oliver*

Brain metastases are the most lethal progression events, in part because the biological processes underpinning brain metastases are poorly understood. There is a paucity of realistic models of metastasis, as current *in vivo* murine models are slow to manifest metastasis. Metabolic and secretory modulators of brain metastases utilizing two models consisting of *in vitro* microfluidic devices are delineated: 1) a blood–brain niche (BBN) chip that recapitulates the blood–brain barrier and niche; and 2) a migration chip that assesses cell migration. Secretory cues provided by the brain niche that attract metastatic cancer cells to colonize the brain niche region are reported. Astrocytic Dkk-1 is increased in response to brain-seeking breast cancer cells and stimulates cancer cell migration. Brain metastatic cancer cells under Dkk-1 stimulation increase gene expression of FGF-13 and PLCB1. Further, extracellular Dkk-1 modulates cancer cell migration upon entering the brain niche.


cases with a median survival of 5–20 months, depending on the subtype.^[1] Treatment of other metastatic sites has improved,^[2] but many treatments do not cross the blood–brain barrier (BBB) or are ineffective at treating brain metastases.^[3] Although a subset of metastatic cancer can extravasate through the BBB, the molecular processes that regulate this are poorly understood. Even though many cancer cells succeed in crossing the BBB, the majority are unable to colonize the brain niche microenvironment and instead die or senesce. According to the classical seed-and-soil hypothesis, for metastatic cancer cells to colonize, they must interact with brain niche components and secretions to promote a hospitable environment.^[4]

The unknown factors contributing to cancer cell death or survival in the brain niche could directly influence the development of therapeutics and are of interest to the cancer community. Two resident cells of the brain niche, astrocytes

1. Introduction

Brain metastasis is the most lethal secondary cancer progression for most tumor types, including breast, and occurs in 10–20% of

T. M. Westerhof,^[+] N. M. Merrill, J. A. Yates, M. Altemus,^[++] L. Bao, Z. Wu, P. J. Ulintz, A. Morikawa, S. D. Merajver, C. R. Oliver
Michigan Medicine
Department of Internal Medicine
Division of Hematology/Oncology
University of Michigan Medical School
Ann Arbor, MI 48109, USA
E-mail: croliver@umich.edu

 The ORCID identification number(s) for the author(s) of this article can be found under <https://doi.org/10.1002/anbr.202200036>.

^[+]Present address: Bio-Rad, Digital Biology Group, Ann Arbor, MI 48109, USA

^[++]Present address: Michigan Medicine, Oncology Clinical Trial Support Unit, University of Michigan, Ann Arbor, MI 48109, USA

© 2022 The Authors. Advanced NanoBiomed Research published by Wiley-VCH GmbH. This is an open access article under the terms of the Creative Commons Attribution License, which permits use, distribution and reproduction in any medium, provided the original work is properly cited.

DOI: 10.1002/anbr.202200036

B. A. Yang, L. Russell, A. J. Miller, C. A. Aguilar
School of Engineering
Department of Biomedical Engineering
University of Michigan
Ann Arbor, MI 48109, USA

M. G. Castro
Michigan Medicine
Department of Neurosurgery
University of Michigan
Ann Arbor, MI 48109, USA

M. G. Castro
Michigan Medicine
Department of Cell and Developmental Biology
University of Michigan
Ann Arbor, MI 48109, USA

and microglia, appear to react to cancer cells entering the brain space and have been detected surrounding brain metastases.^[5] However, limited data is available to understand the influence of secretory molecules emanating from the brain niche cells in regulating brain metastasis.

Astrocytes are vital regulators of homeostasis in the normal brain niche and support the roles of endothelial and pericyte cells in forming the BBB through multimodal interactions.^[6] Astrocytes adopt reactive phenotypes upon sensing homeostatic deviations, such as brain injury or infection.^[7] Reactive astrocytes in the presence of cancer cells have recently emerged as cellular components complicit in the formation of brain metastases.^[6,8] A partial panel of astrocyte secretions produced in reaction to cancer cells in the brain have been identified.^[9] Brain metastatic (BR) cancer cells increase reactive astrocytic secretion of plasminogen activators (PA), tissue-PA (tPA), and urokinase (uPA). These PAs induce high levels of plasmin in the brain niche, which promote cell death in many cancer cells reducing BBB colonization rates. To thrive in the brain niche with elevated PAs, BR cancer cells secrete PA inhibitors, SerpinI1, and SerpinB2.^[10] In contrast, in a beneficial manner, astrocytic secretion of IL-6 and MCP-1 (CCL-2) influences extravasated cancer cells to form tumors in proximity to the BBB, forming blood–tumor barriers (BTB) through S1P3 signaling.^[11]

Microglia are the resident macrophages of the brain niche that actively survey the central nervous system for damage and infectious agents, including cancer cells.^[12] Like astrocytes, microglia adopt different phenotypes depending on the environment. Classical M1 microglia destroy infiltrating tumors through production of cytotoxic factors and proinflammatory cytokines (IL-1 β , TNF- α , ROS, IFN- γ , IL-12). In contrast, activated M2 microglia elicit a protumor response through secretion of anti-inflammatory cytokines, immunomodulatory mediators, and growth factors (IL-10, TGF- β , VEGF, and MMPs).^[13] In the context of brain metastasis, heterogeneous populations of microglia surround and infiltrate tumors.^[14]

In this study, we utilized both a migration and a blood–brain niche (BBN) microfluidic chip to characterize alterations to the brain niche and cancer cell metastatic progression. Our goal is to characterize phenotypic and secretory cues provided by individual cellular residents of the brain niche, astrocytes and microglia, that attract metastatic cancer cells. We characterized these behaviors in two breast cancer cell lines, MDA-MB-231 (TNBC) and JIMT1 (Her2+), as well as two BR derivatives of these lines, MDA-MB-231-BR and JIMT1-BR.^[15] Fluctuations in metastatic cancer cell secretions (cytokines and metabolites) after stimulation with individual brain niche cellular or secretory components are used to establish secretory profiles of tumor cells that promote brain niche remodeling. In contrast, variations in astrocyte, microglia, and brain microvascular endothelial cell secretions when stimulated with cancer cellular or secretory components are used to identify unique cytokine and metabolite profiles. We examine if individual secretions can be inhibited to modulate remodeling of the brain niche. Specifically, we observe if neutralization of Dkk-1 secretion alters the cancer cell-induced remodeling within the brain niche. Finally, we examined the impact on two genes (FGF-13, PLCB1) that are important to Dkk-1-related pathways and study their impact on cell migration in Dkk-1 gradients.

2. Results

2.1. Astrocyte Cells Promote Metastatic Cancer Cell Extravasation through the BBB

To examine the influence of astrocytes and microglia cells on cancer cell extravasation through the BBB, we utilized an established microfluidic BBN chip to observe and characterize cancer cell extravasation and colonization of the BBN (**Figure 1a**).^[16] The details of the BBN chip and the method used for analysis (confocal tomography) are discussed in the Experimental Section and Supporting Information. All the data in Figure 1 is derived by measuring the positions (centroids) of cancer cells and brain resident cells (astrocytes and microglia) relative to the BBB (endothelial cells) in the device. These were measured from fluorescent 3D confocal images. To image the entire device, a motorized stage was used to stitch images from 9 adjacent fields of view along the 14 mm length of the channel. At each location, 50 images were taken at 10 μ m steps along the z-axis. The depth of the device is 500 μ m with 200 μ m imaged above the BBB membrane and 300 μ m below it. Taking \approx 50 images at 10 μ m steps enabled accurate 3D volumetric reconstruction of the cells within the device. The cells were segmented and measured as described in the supplemental section and in prior work. This synthetic BBN system was utilized to test the ability of astrocytes or microglia to attract parental and BR cancer cells to the brain region after 2 and 9 days of interaction (**Figure 1**).

Figure 1c displays the interaction between individual astrocytes and cancer cells represented as a density plot (parental: MDA-MB-231, JIMT1 and BR: MDA-MB-231-BR, JIMT1-BR) whereas **Figure 1b** describes how to interpret the plot shown in **Figure 1c**. The X-axis shows the position of the cancer cells relative to the BBB while the Y-axis shows the position of the astrocytes or microglia relative to the BBB. Each measurement is for a pair of cancer cells and astrocytes in the device. Cells were paired if the cancer cell was directly above or below a nearby astrocyte. In this way, the relationship of the effect of astrocytes on cancer cells is observed locally and then transformed into a 2D plot with the BBB as a reference. These plots are divided into four quadrants that describe where in the BBN device the cells are located. Quadrant 1 shows cancer cells in the brain side of the device and astrocytes on the flow chamber side. Quadrant 2 shows cancer and astrocyte cells in the brain side of the device. Quadrant 3 shows cancer and astrocyte cells on the flow chamber side of the device. Finally, quadrant 4 shows cancer cells in the flow chamber and astrocyte cells in the brain side of the device. The proximity of the measured interaction can be visualized by the distance away from the short, dotted diagonal line. When the two cells touch, they will be plotted on the diagonal line and the further apart they get from each other, the further from the diagonal line they will be. The red overlays in quadrants 1 & 2 show when cancer cells are in the lower 50% of the brain chamber. The blue overlays in quadrants 2 & 4 show when the astrocyte cells are in the lower 50% of the brain chamber. In the figure, the endothelial barrier is represented by the long-dashed lines. Because this is a density plot of pairs of cancer cells and astrocytes from along the length of the device, we can appreciate the overall change in how cancer cell type alters the positions of the astrocytes and vice versa.

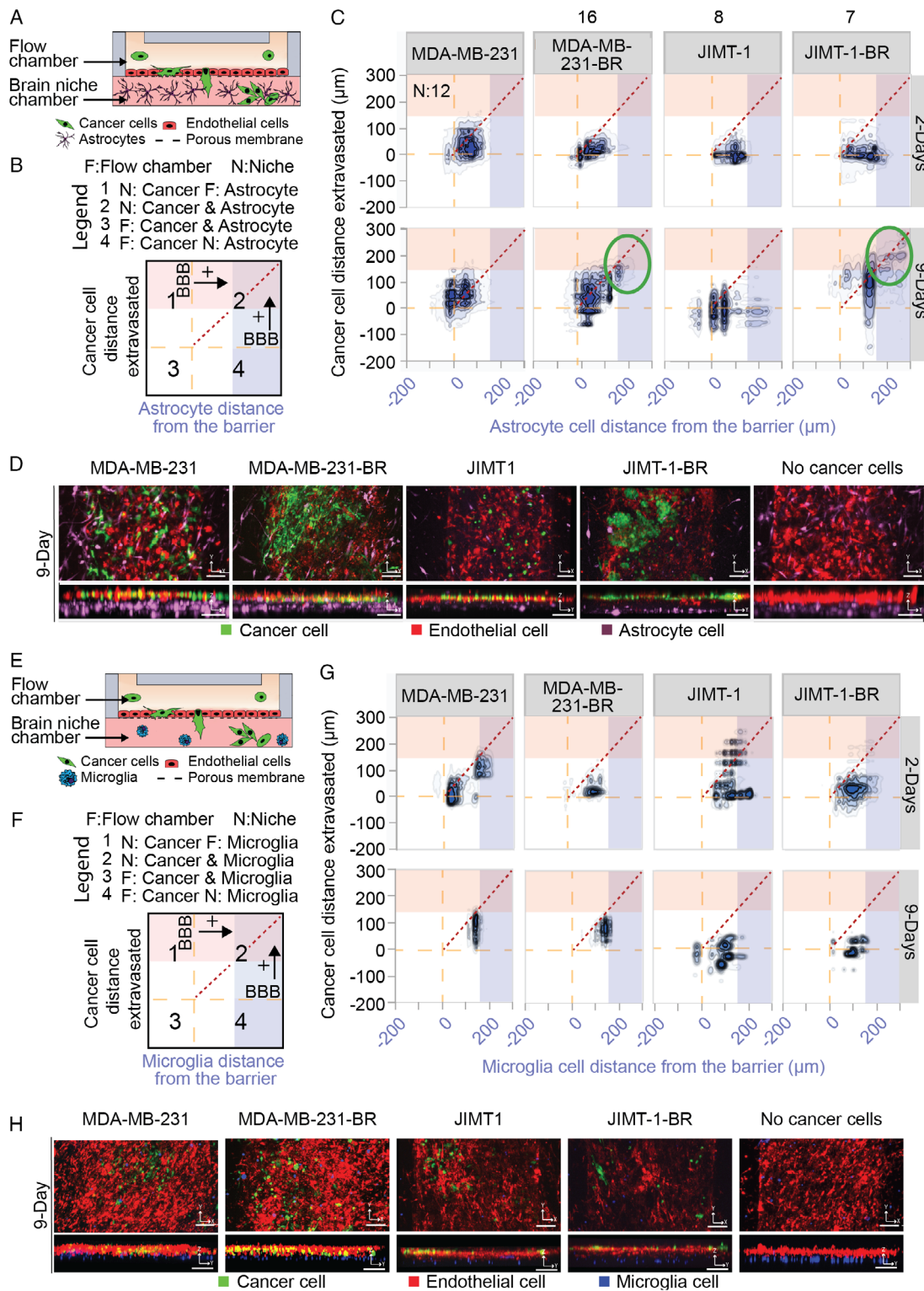


Figure 1. BR cancer cells extravasate toward astrocyte cells. A,E) Schematic of a BBN with (A) astrocytes or (E) microglia in the brain niche chamber. Cancer cells in the top flow chamber interact with the BBN for 2- and 9 days. B,F) Legend for (C) and (G) respectively. Each quadrant shows interactions between cancer cells and brain niche cells. The yellow dashed line represents the endothelial barrier. Red and blue overlay denote a distance from barrier $> 150 \mu\text{m}$. (C,G) 2D density plot of cancer cell and (C) astrocyte or (G) microglia interaction for MDA-MB-231, MDA-MB-231-BR, JIMT-1, JIMT-1-BR for 2 and 9 days. (D,H) Representative fluorescent confocal images of cancer cells in BBN chips with (D) astrocytes or (H) microglia after 9 days. Images are in the XY and YZ planes, scale bar = $125 \mu\text{m}$. A list of replicates per condition is given in Table S1, Supporting Information.

Astrocyte cells supplemented in the niche uniquely attracted some MDA-MB-231-BR and JIMT1-BR and formed distinct clustered micrometastases spanning the niche after 9 days of culture (Figure 1c circled region). The MDA-MB-231-BR average distance extravasated across the time points did not significantly vary, but the overall distribution of metastatic cancer cells differed significantly between BR and parental cancer cells. Most parental MDA-MB-231 cells remained concentrated at the endothelial barrier with a small subset of cells that migrated deeply into the brain niche. JIMT1-BR and parental JIMT1 also maintained proximity to the endothelial barrier after 2 days (Figure 1). However, after 9 days, both MDA-MB-231-BR and JIMT1-BR exhibited a large proportion of fully extravasated cells into the brain niche compartment and contained subsets of migratory cells positioned farther within the brain niche. The distributions of distance extravasated measurements of MDA-MB-231 and JIMT1 cancer cells were significantly different when comparing between 1) BR and parental lines; and 2) across timepoints (Figure 1c).

Simultaneous monitoring of the astrocytes revealed they reposition themselves within the BBN. The presence of BR MDA-MB-231-BR cells influenced astrocytes toward the endothelial barrier, touching the extravasated MDA-MB-231-BR cancer cells at 2 days and sustaining contacts after 9 days (Figure 1c). Astrocytes appeared to minimize contact with JIMT1-BR. JIMT1 were positioned the farthest away from the barrier at both 2 days and 9 days (Figure 1c). Figure 1d shows representative images at 9 days; images with an enlarged z-axis are provided in Figure S1a, Supporting Information, for 2 and 9 days.

2.2. Microglia Cells Influence Metastatic Cancer Cells to Remain in Proximity to the BBB

Using the same methodology (Figure 1e–h), we sought to describe the effects of microglia on cancer cell metastasis. In contrast to astrocytes, there was limited remodeling of the microglia in the BBN chips containing microglia cells (Figure 1g). For the MDA-MB-231 cells, the microglia cells transition from two groups (13 μm and 150 μm) to a single cluster at (150 μm) at 9 days. However, the MDA-MB-231 cells have reduced their dispersion at 2 days. The JIMT-1 parental line does show a larger change in the cancer cells moving

from deep within the device toward the endothelial layer. Contrasting this to the MDA-MB-231-BR cells, the microglia again move toward 150 μm away from the BBB with exceptions. The JIMT-1-BR tighten behavior but show no major changes between 2 and 9 days. It is also observed that the microglia reposition into thin layers in most cases. Figure 1h. shows representative images at 9 days; images with an enlarged z-axis are provided in Figure S1b, Supporting Information, for 2 and 9 days.

2.3. BBN Secretions Influence Cancer Cell Migration and Extravasation

Given the differences in cancer cell extravasation when exposed to astrocyte and microglia cells, we hypothesized that basal

secretions within the brain niche alone may influence cancer cell migration and extravasation. To examine the effect of brain niche cell secretions on metastatic breast cancer cell migration, we used a microfluidic chip that permits quantitative monitoring of linear cell migration,^[17] which is described in the supplemental data (Figure S2a, Supporting Information) and Experimental Section. We found astrocyte secretions could alter migratory behavior or MDA-MB-231-BR cells.

We next used a microfluidic BBN chip composed of a cell-free collagen brain niche chamber infused with either basal astrocyte or microglia secretions (Figure 2a,b). This created a brain niche rich in cytokines protected by an endothelial cell barrier. We monitored cancer cell extravasation toward astrocyte or microglia secretions after both 2 and 9 days. Controls using nonconditioned media are shown in Figure S3, Supporting Information.

After 2 days, astrocyte secretions promoted cancer cell extravasation of both brain-seeking and parental cancer cell types, with most of the cancer cells surrounding the endothelial barrier (Figure 2c). At 9 days, the parental MDA-MB-231 cells moved toward the barrier while the brain tropic cells migrated deeper into the device and developed into distinct subpopulations. In contrast, the JIMT-1 parental and JIMT-1-BR converged toward the endothelial barrier. However, the JIMT-1-BR maintained two population peaks. The trend towards a spherical shape (sphericity) increased for all four cell types between 2 and 9 days (Figure 2e).

Parental MDA-MB-231 and MDA-MB-231-BR cells cultured in BBN chips with microglia secretions at 2 days behaved similarly to astrocyte secretions clustering around the barrier with the brain tropic cells closer to the barrier and showed qualitatively similar, but less aggressive, divergence at 9 days (Figure 2d). JIMT-1 cells however diverge in the presence of microglia secretions with brain tropic cells, by migrating deeper into the device in aggregate (Figure 2d). All cell types increased in sphericity, but differed at 2 days from the behavior observed in the presence of astrocyte secretions (Figure 2f). Representative images of each condition are shown in Figure 2g,h for astrocyte and microglia conditions, respectively. Enlarged images in the z-direction are provided in Figure S4, Supporting Information.

We extracted counts of BBN-relevant micrometastasis or clusters of cancer cells in astrocyte and microglia secretions (Figure 3a,b). The range of extravasation for the clusters is smaller than the single cells (Figure 3c,d). We also observed a wide variation in the number of clusters for the astrocyte secretion condition, triplicate experiments between 128 and 1845 extravasated clusters. Parental MDA-MB-231 cells had a broader set of cluster positions while JIMT-1 cells were much more concentrated around the barrier. However, there were small groups at 2 days of deeply advancing clusters. Sphericity of clusters cultured in astrocyte secretions revealed clusters that are significantly less spherical than individual cells (Figure 2e vs 3e). By 9 days, the brain-seeking cell clusters for both brain tropic cell lines are more spherical than the parental cell clusters (Figure 3e).

Interestingly, in the presence of microglia secretions, the clusters for both cancer cell types cluster around the barrier (Figure 3d) yet maintain a small shift below the barrier for MDA-MB-231-BR and JIMT-1-BR cell types at 9 days compared

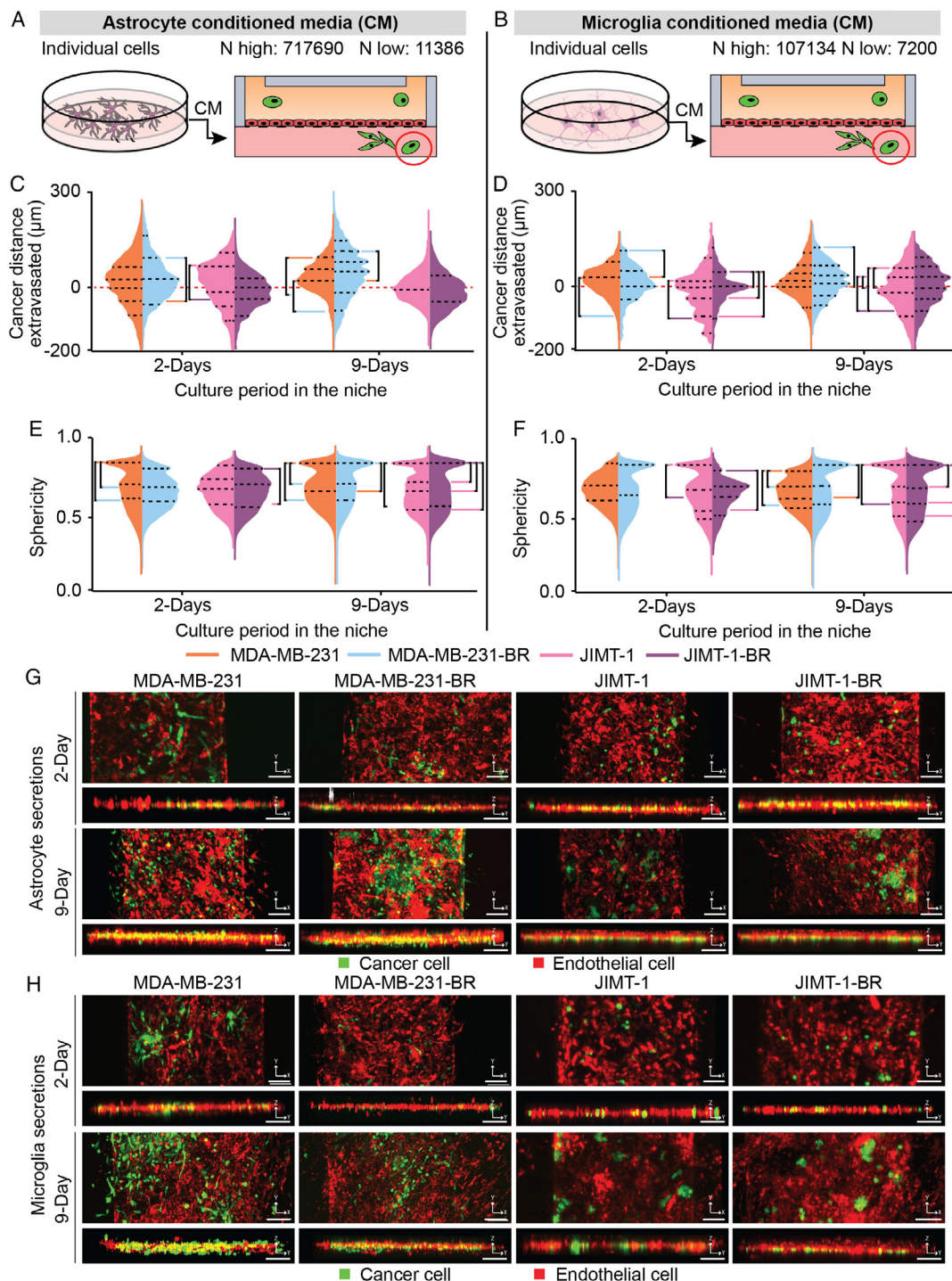


Figure 2. Astrocyte and endothelial secretions influence BR cancer cell migration. A,B) Depiction of how (A) astrocyte- and (B) microglia-conditioned media was collected and placed in the device. The highest (N highest) and lowest (N lowest) count of cells from all replicates and conditions. C,D) Cancer cell positions in BBN chips with (C) astrocyte and (D) microglia secretions plotted as distance (µm) to the endothelial barrier (0 µm). E,F) Sphericity of cancer cells in BBN chips with (E) astrocyte and (F) microglia secretions. G,H) Representative fluorescent confocal images of cancer cell extravasation in µBBN devices infused with (G) astrocyte or (H) microglia secretions after 2 and 9 days, scale bar 125 µm. (C–F) $p < 6.25 \times 10^{-4}$ determined by Mann–Whitney significance tests with a Bonferroni correction. A list of replicates per condition is given in Table S1, Supporting Information.

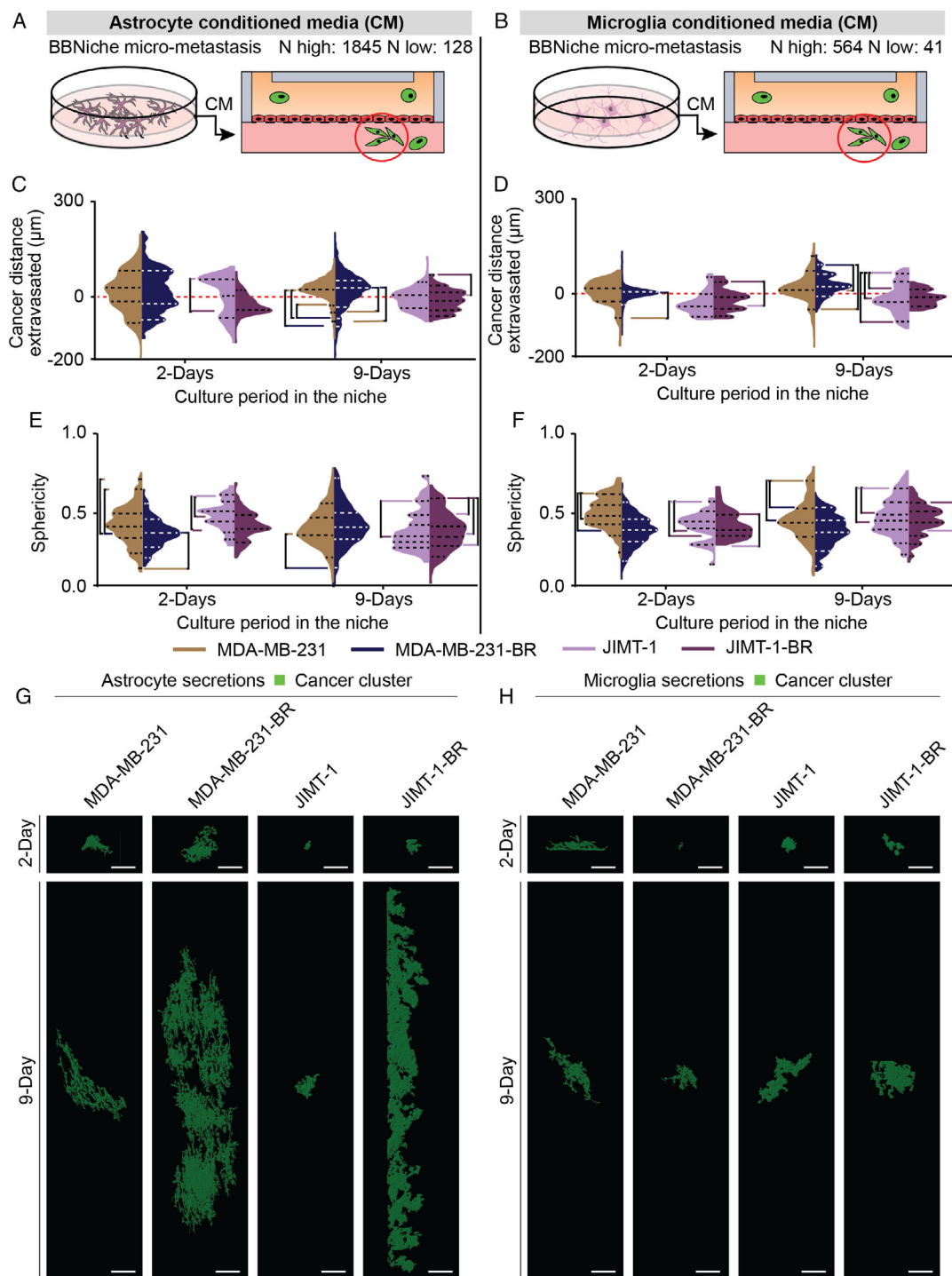


Figure 3. Astrocyte and endothelial secretions influence brain-niche micrometastasis migration. A,B) Depiction of how (A) astrocyte- and (B) microglia-conditioned media was collected and placed into the device. The highest (N highest) and lowest (N lowest) count of cells from all replicates and conditions. C,D) Cancer cell BBN micro-metastasis positions in BBN chips with (C) astrocyte and (D) microglia secretions plotted as distance (μm) to the endothelial barrier (0 μm). E,F) Sphericity of cancer cell BBN micrometastasis in BBN chips with (E) astrocyte and microglia (F) secretions. G,H) Rendering of the largest BBN micrometastasis selected from random devices at 2 days and 9 days for (G) astrocyte secretions and (H) microglia secretions. Scale bars are 200 μm . (C–F) $p < 6.25 \times 10^{-4}$ determined by Mann–Whitney significance tests with a Bonferroni correction. A list of replicates per condition is given in Table S1, Supporting Information.

to the parental cell types. The JIMT-1-BR cells at 9 days exhibit lower-variance clusters when in microglia secretions than in the astrocyte secretions (Figure 3c,d). Compared to astrocyte secretions, dramatic shifts in cluster sphericity in the microglia condition occurred (Figure 3e–f). MDA-MB-231 parental clusters are initially more spherical at 2 days but shift at 9 days toward MDA-MB-231-BR clusters (Figure 3f). However, MDA-MB-231-BR clusters have a tail of nonspherical shapes. Inverse behavior was observed in the JIMT-1 cells. The JIMT-1-BR clusters become more spherical by 9 days, which is also the reverse of their behavior in the astrocyte secretions (Figure 2f vs 3f).

Representative images of the largest cluster found in a randomly selected channel for each cancer cell type and culture time condition are shown in Figure 3g,h for astrocyte- and microglia-conditioned media, respectively. The clusters of brain tropic cells are larger than those of the parental line in astrocyte secretions than in microglia secretions.

2.4. The Cytokine Response of the Brain Niche is Influenced by Interaction with MDA-MB-231-BR

Astrocyte, microglia, and endothelial cells are known to secrete cytokines within the normal brain niche to maintain homeostasis and to have the ability to rapidly fluctuate in response to invasive pathogens or damage.^[5,18] Given the unique astrocytic and microglial reorganization in the context of BR cancer cells, we examined the secretory cytokine profiles of astrocytes and endothelial cells dependent on cancer cell interaction using dot blot arrays (Figure 4b). ELISA showed astrocytes increased secretion of IL-6, IL-8, Dkk-1, CXCL-5, Chitinase 3-like 1, VCAM-1, SerpinE1, and MCP-1 when stimulated with MDA-MB-231-BR (Figure 4c, S5a, Supporting Information). No significantly increased endothelial secretions were detected with MDA-MB-231-BR stimulation (Figure 4d, S5b, Supporting Information) using ELISA. A total of nine cytokines were

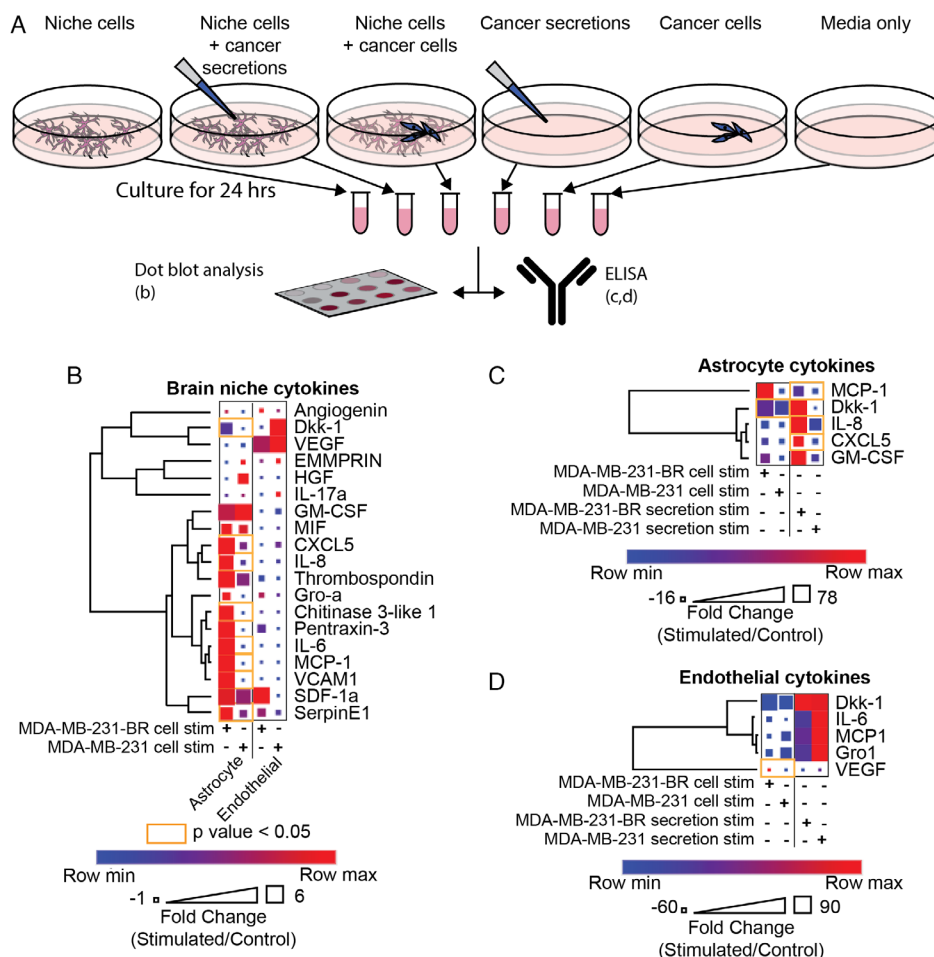


Figure 4. Brain niche cytokine profiles are altered after interaction with cancer cells. A) Schematic showing collection of conditions used for cytokine profiling and distribution to a dot blot assay and ELISA. B) Human XL cytokine dot blot array results for astrocyte and endothelial cell secretions, when stimulated with either MDA-MB-231-BR or parental MDA-MB-231 and normalized to a nonstimulated control. Heatmap colors indicate row comparisons of each cytokine level, blue (low) to red (high). Square size indicates overall cytokine protein levels. C,D) ELISAs of (C) astrocyte or (D) endothelial secretions after stimulation with either cancer cells or paired secretions were normalized to unstimulated secretion controls. For all assays, orange outlines indicate statistically significant comparisons and *t*-tests with Holm–Šidák multiple comparisons correction were utilized. The assays were performed in triplicate.

significantly elevated in microglial secretions when stimulated with MDA-MB-231-BR: Angiogenin, Dkk-1, GM-CSF, IL-8, Gro-a, Chitinase 3-like 1, IL-6, MCP-1, and SerpinE1 (Figure S5c, S5d, Supporting Information) using ELISA. However, the relative quantity of microglia secretion was lower compared to the output of cytokines by the astrocytic cytokines; thus, subsequently, the study focused on understanding the influence of astrocytic secretions on cancer cell metastasis.

We employed ELISAs as an orthogonal approach to validate and quantify the salient cytokines identified using dot blot arrays. Astrocytes or endothelial cells were stimulated with either cancer cells or their corresponding secretions. When astrocytes were stimulated with MDA-MB-231-BR cancer cell secretions alone, they significantly increased secretions of cytokines MCP-1, IL-8, and CXCL5, compared to stimulation with MDA-MB-231-BR cells, parental MDA-MB-231 cells, or parental MDA-MB-231 secretions (Figure 4c). Astrocytic stimulation with physical MDA-MB-231-BR cells, but not their secretions, only increased the astrocytic secretion of Dkk-1. Under stimulation with MDA-MB-231-BR cells but not with parental MDA-MB-231 cell stimulation, endothelial cells significantly increased the secretion of VEGF (Figure 4d). Endothelial stimulation with cancer secretions alone promoted an increase in cytokine production whose levels were not significantly different between stimulation with MDA-MB-231-BR and MDA-MB-231 secretions.

2.5. MDA-MB-231-BR and Parental MDA-MB-231 Cancer Cells Differentially Modulate Cytokine Profiles in Response to BBN Stimulation

Cancer cell extravasation across the BBB and colonization of the brain niche require cancer cells to remodel the brain niche to promote their survival. We hypothesized paracellular communication through cytokines as a means cancer cells use to modify the brain niche into a suitable metastatic environment. We identified secretions from cancer cells with and without direct interaction from individual brain niche cells (astrocytes, microglia, or endothelial cells) using dot blot arrays (Figure S6a, Supporting Information) to profile cytokines from the cancer cells which promote metastasis. We observed significantly different levels of IL-6, SerpinE1, and Dkk-1 cytokines secreted by MDA-MB-231-BR when stimulated with astrocytes or microglia (Figure S6b, Supporting Information).

2.6. Dkk-1 Influences BR Cancer Cell Migration and Extravasation across the BBB

As astrocytic and endothelial secretions promoted a migratory phenotype (Figure S2, Supporting Information), we postulated that a regulated and prevalent cytokine may influence cancer cell extravasation across the BBB. Dkk-1 was a cytokine that astrocytic and endothelial components upregulated in the presence of MDA-MB-231-BR stimulation. Dkk-1 is a known Wnt signaling inhibitor and influencer of cancer cell dormancy.^[19] Dysregulation of Wnt signaling has commonly been implicated in cancer progression.^[20] Thus, we interrogated the influence of

Dkk-1 on metastatic cancer cell migration and extravasation into the brain niche and on linear 2D migration devices.

To uncover the role of astrocytic Dkk-1 secretion on cancer cell migration in 2D, MDA-MB-231-BR cells were subject to analysis in our microfluidic migration chip. Two Dkk-1 gradients were assessed alongside controls: 1) an increasing concentration of Dkk-1 in serum-free media (SFM) to assess the effects of Dkk-1 as a chemoattractant; and 2) with Dkk-1 provided in SFM as a stimulus to the cancer cells across the migration chip, with 10% FBS as an external chemotactic gradient. Chemotactic gradients of SFM-Dkk-1 (20 ng mL⁻¹) do not promote MDA-MB-231-BR or MDA-MB-231 cancer cell migration (Figure 5a–c). Instead, Dkk-1 acted as a stimulatory factor and enhanced cancer cell migration toward external gradients of FBS, compared to FBS alone (Figure 5a–c). Thus, Dkk-1 does not act alone in a chemotactic manner; instead, cancer cells adopt a migratory phenotype due to direct stimulation of Dkk-1. No statistically significant cell growth was detected over 48 h in all gradient conditions (Mann–Whitney *t*-tests with Bonferroni correction, $p < 6.25 \times 10^{-3}$).

To confirm Dkk-1 role in the BBN chip, after introducing cancer cells, we used 10 μg mL⁻¹ of Dkk-1 neutralization antibody in the brain niche space of an astrocyte-laden microfluidic BBN chip twice daily. After 2 days cancer cell migration within the brain niche was markedly decreased in the μBBN chip with Dkk-1 neutralization (Figure 5d–h), we overlaid the response of the cancer cell distance extravasated and astrocyte cell distance from the barrier shown in Figure 1 (blue) with the results from cells cultured in the Dkk-1 neutralization antibody (red) (Figure 5e). All MDA-MB-231-type cells moved away from the dashed diagonal line indicating differential remodeling away from each other (Figure 5e). The parental MDA-MB-231 cells do not migrate as deeply into the device and the astrocyte cells move further from the barrier. The MDA-MB-231-BR cells divide into groups where astrocytes move away from the barrier as cancer cells infiltrate. This results in a similar shift in distance but by a different mechanism. The JIMT-1 parental line shows the astrocytes congregating at 100 μm away from the barrier but a large proportion of cancer cells have moved back into the flow side of the chamber. Finally, the JIMT-1-BR cells exhibit mixed behavior where many astrocytes group 150 μm away from the barrier, but a second group moved toward the tumor cell location.

The average distance between cancer cells in astrocytic BBN chips with or without Dkk-1 neutralization (Figure 5f–g) confirms these interpretations. The kernel estimate histogram of an untreated control was subtracted from the sample treated with the Dkk-1 neutralization antibody and plotted to show the change in cancer to astrocyte distance. In the presence of Dkk-1-neutralizing antibody (low Dkk-1 condition), the MDA-MB-231 parental line and astrocytes are ≈150 μm apart on average. A similar trend is seen for the MDA-MB-231 brain tropic cells, but the cells are further apart (≈175 μm). The JIMT-1 parental line also shifts away from the original bulk position of 50 μm to two subsets positioned at 150 and 175 μm. However, the brain tropic JIMT-1 cells have two small populations that move apart but have a broader set of cells across distances. Finally, we show representative images of the device with and without the Dkk-1-neutralizing antibody treatment in Figure 5h.

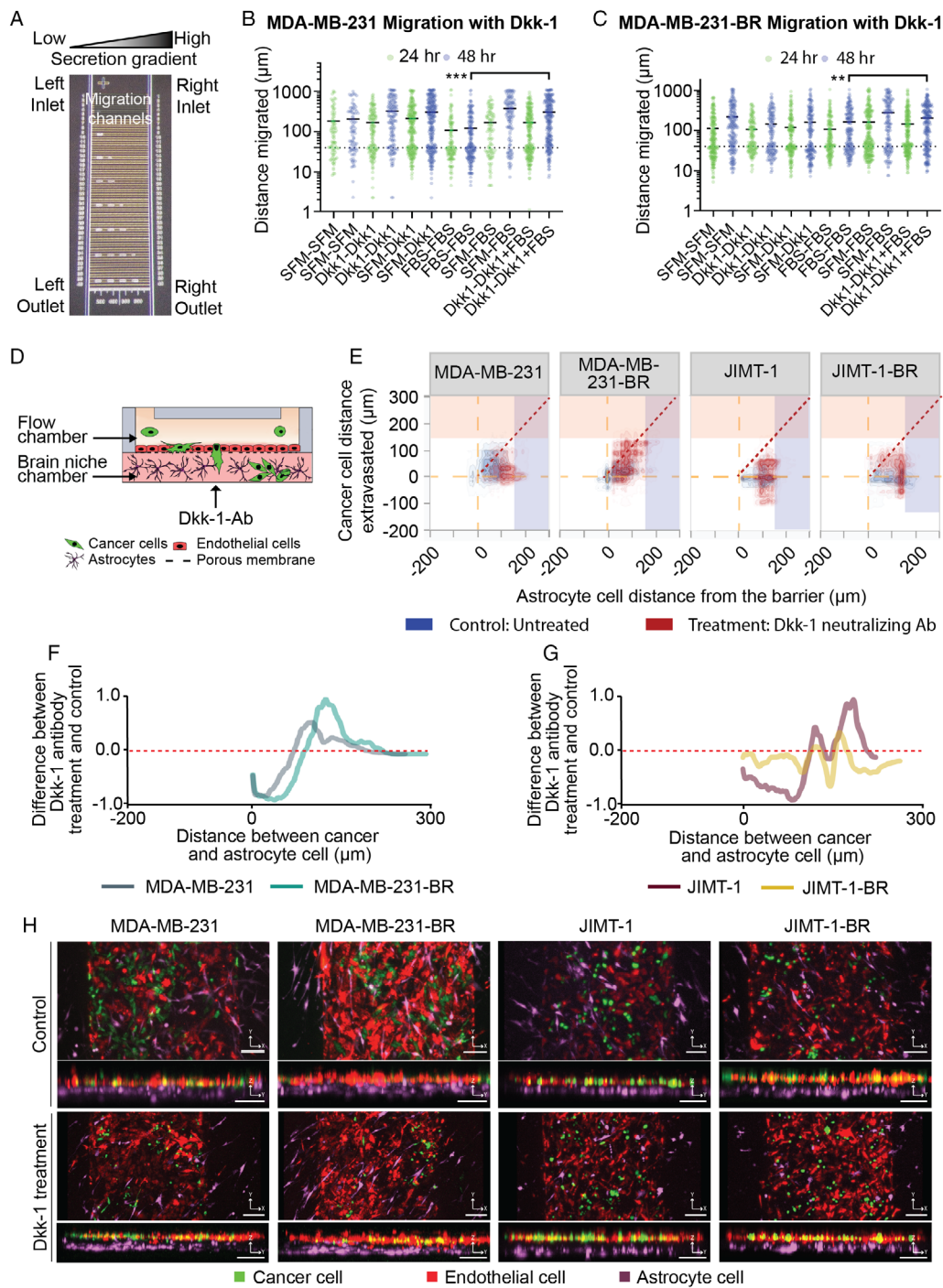


Figure 5. The Dkk-1 cytokine influences cancer cell extravasation and interaction with astrocytes. A,B) Purified Dkk-1 was tested as a chemoattractant/stimulant for cancer cell migration using microfluidic devices. (A) Image of the microfluidic migration chip. Details in the supplemental methods. (B) MDA-MB-231 and C) MDA-MB-231-BR cell migration in chemotactic gradients using combinations of: SFM, FBS, and 20 ng mL⁻¹ Dkk-1. D–H) Cancer cells in BBN chips with astrocytes treated with or without Dkk-1 neutralization antibody (10 μg mL⁻¹) for MDA-MB-231, MDA-MB-231-BR, JIMT-1, JIMT-1-BR. (D) Dkk-1 -neutralizing antibody was administered in the brain niche chamber. (E) Distance (μm) between the cancer cells and the endothelial barrier in BBN chips compared to astrocyte cell position treated with or without Dkk-1 neutralization antibody (10 μg mL⁻¹) for MDA-MB-231, MDA-MB-231-BR, JIMT-1, JIMT-1-BR. (F–G) Difference between the samples treated with Dkk-1 neutralizing Ab and untreated samples for (F) MDA-MB-231-BR and MDA-MB-231 cells, and (G) JIMT-1-BR or JIMT-1. (H) Confocal images of cancer cell extravasation into BBN chips treated with 10 μg/mL Dkk-1 neutralization antibody, scale bar 125 μm. (B–C) $^{***}p < 6.25 \times 10^{-3}$, $^{***}p < 6.25 \times 10^{-4}$, Mann–Whitney significance tests with a Bonferroni correction. A–B was performed with three biological replicates each with three technical replicates. Refer to Table S1, Supporting Information for list of replicates per condition in (D–H).

2.7. BR Cancer Cell Metabolism is Rewired when Stimulated with Brain Niche Secretions

The influence of the brain niche on cancer cell migration and extravasation suggested that contact with brain niche secretions alters cancer cell metabolism. Changes in the extracellular metabolites of MDA-MB-231-BR and MDA-MB-231 under stimulation with brain niche secretions were quantified using mass spectrometry and NMR.

Alterations of the secreted metabolome were observed in amino acids (Figure 6a). The MDA-MB-231-BR secreted the highest levels of phenylalanine, succinate, and alanine when stimulated with brain niche secretions (Figure 6b). In contrast, the highest parental MDA-MB-231 secreted metabolites including histidine when stimulated with astrocyte or microglia secretions and valine when stimulated with endothelial secretions (Figure 6b). The same measurements are provided for the metabolite changes in the brain niche cells (astrocytes, microglia, and endothelial cells) due to stimulation from the MDA-MB-231 and MDA-MB-231-BR secretions (Figure S8, Supporting Information).

The MDA-MB-231-BR and MDA-MB-231 enriched several metabolic pathways under stimulation of brain niche cell secretions including (Figure 6c,d, S9, Supporting Information) urea cycle; aspartate metabolism; glucose-alanine; alanine metabolism; aspartate metabolism; glycine and serine metabolism; Warburg effect; valine, leucine, and isoleucine degradation; and glutathione metabolism. Astrocyte secretion stimulation of MDA-MB-231-BR and MDA-MB-231 uniquely increased arginine and proline metabolism compared to stimulation. MDA-MB-231-BRs and MDA-MB-231s stimulated with endothelial secretions promoted pathway enrichment of ammonia recycling, glutamate metabolism, amino sugar metabolism, and ethanol degradation. Microglia secretions did not promote any unique metabolomic pathways compared to astrocyte or endothelial secretions shared in both MDA-MB-231-BRs and MDA-MB-231s.

The MDA-MB-231-BR extracellular metabolomic profile under stimulation of brain niche cell secretions commonly expressed pathway enrichment of glutamate metabolism; arginine and proline metabolism; and amino sugar metabolism. When MDA-MB-231-BR are stimulated with astrocyte secretions, the MDA-MB-231-BR uniquely increase: ammonia recycling; glutamate metabolism; arginine and proline metabolism; and amino sugar metabolism (Figure 6d). With microglia secretion stimulation, the pathways unique to MDA-MB-231-BR were: glucose-alanine cycle; Warburg effect; glycine and serine metabolism; amino sugar metabolism; alanine metabolism; glutamate metabolism; ethanol degradation; glutathione metabolism; arginine and proline metabolism; transfer of acetyl groups into mitochondria; and valine leucine and isoleucine degradation. Endothelial secretion stimulation of MDA-MB-231-BR resulted in signaling of arginine and proline metabolism; transfer of acetyl groups into mitochondria; and methylhistidine metabolism.

No shared metabolic pathways were enriched in the parental MDA-MB-231 under brain niche cell secretions. The MDA-MB-231s under astrocyte secretion stimulation increased signaling of: ethanol degradation; transfer of acetyl groups into mitochondria; tryptophan metabolism; and folate metabolism. Endothelial

secretions stimulated one unique metabolic pathway in MDA-MB-231s compared to MDA-MB-231-BR: arginine and proline metabolism. Microglia secretions did not yield enrichment of pathways that were uniquely expressed by the MDA-MB-231s and not MDA-MB-231-BR. Overall, interactions with the niche cells, especially astrocytes, yielded increases in critical amino acid metabolic pathways especially in brain trophic cells compared to parental controls, pointing to modulation of these pathways as reasonable potential avenues to help control metastatic growth in the brain niche.

2.8. Gene Expression Profiling of MDA-MB-231-BR and MDA-MB-231 under Dkk-1 Stimulation

To characterize the cancer cell response to Dkk-1 at the molecular level, NanoString PanCancer Pathways gene expression profiles were compared between MDA-MB-231-BR and MDA-MB-231 with and without Dkk-1 stimulation for 24 h. A total of 30 significant differentially expressed genes were found to be expressed in the MDA-MB-231-BRs under Dkk-1 stimulation (Figure 7a,b). They showed increased expression of FGF-13, PLCB1, and MYC and decreased expression of ITGB4, NGF, and PRKX. NanoString nSolver identified Wnt, Ras, PI3K, and MAPK signaling pathways as utilized by the MDA-MB-231-BRs under Dkk-1 stimulation (Figure 7c). Further detailed data are shown in Figure S10, Supporting Information.

FGF-13 was knocked down in both MDA-MB-231 cells to determine if it plays a pivotal role in regulating the effect of Dkk1 in the tumor microenvironment. The pGIPZ and FGF-13 knockdown variants were seeded into the migration device discussed in Figure S2, Supporting Information, under the same conditions before being imaged and analyzed at 24 and 48 h. First, to confirm the knockdown reduced Dkk1 expression under astrocytic stimulation, ELISA (Figure 7d) was performed on the FGF-13 knockdown and controls. The expression levels were reduced by an order of magnitude. The images in Figure 7e show that MDA-MB-231-BR and MDA-MB-231 cells exhibited different morphologies with the MDA-MB-231-BR cells elongated under an SFM-Dkk1 gradient. Finally, Figure 7f,g shows the relative average distance FGF-13 shRNA knockdown cells migrated compared to pGIPZ scramble at 24 and 48 h, respectively. The error bars show the standard error. Significance was tested by *t*-tests with Holm-Šidák multiple comparison tests between the parental and brain-seeking cells. At 24 h, the brain-seeking cells differed from the parental cells but also had reduced migration when fully stimulated with Dkk1-Dkk1 relative to the control. In contrast, the parental knockdown was often more migratory than the control. At 48 h these differences often resolve with both cell types migrating in a similar manner to the control in the presences of Dkk1.

3. Discussion

3.1. Astrocyte Cells and their Secretions Are Integral for Brain Metastasis

While previous work has identified the basic behavior of parental and brain trophic cells inside of the BBN, little is known about the

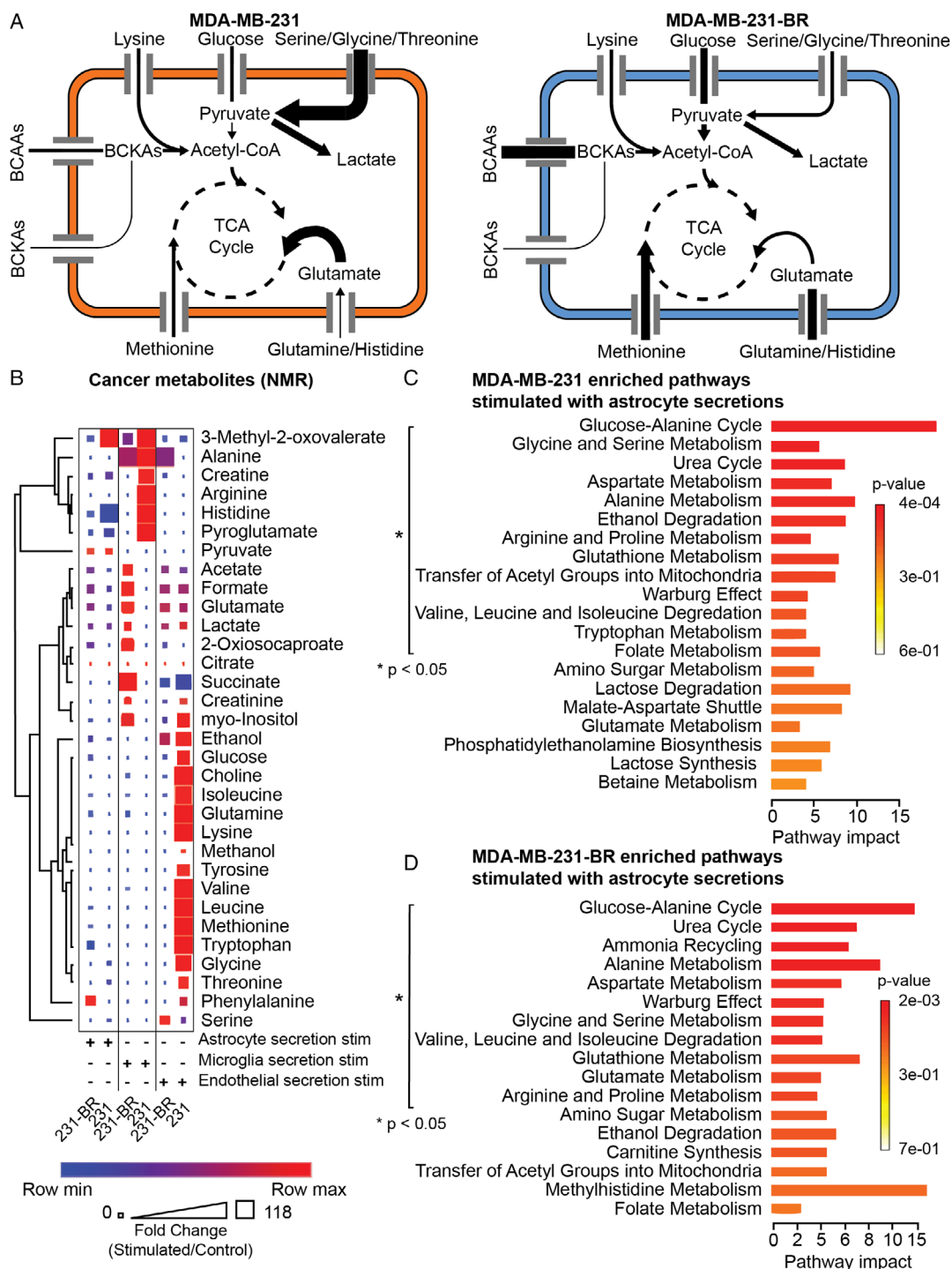


Figure 6. Cancer cell metabolism is influenced by brain niche secretions. A) Summary of changes in metabolic pathway enrichment between MDA-MB-231 and MDA-MB-231-BR cells in the presence of astrocytes. B) Cancer secretion metabolites quantified using NMR. Each cancer type was stimulated with brain niche secretions. Heatmap colors indicate row comparisons of each metabolite level; blue (low) to red (high). The size of each square indicates overall metabolite levels. C, D) Metabolic pathway impact in (C) MDA-MB-231 or (D) MDA-MB-231-BR under stimulation with astrocyte secretions, $p < 0.05$. Metaboanalyst pathway impact. NMR was performed once.

interaction between the cancer cells and the individual cell components within the brain.^[21] A great deal of work has shown that the tumor cells can evade the BBB although a mechanism is not

fully understood.^[22] Recent studies have begun to elucidate the role of astrocyte cells on brain tumor and brain metastasis development.^[23] In murine models, astrocytes are responsible for

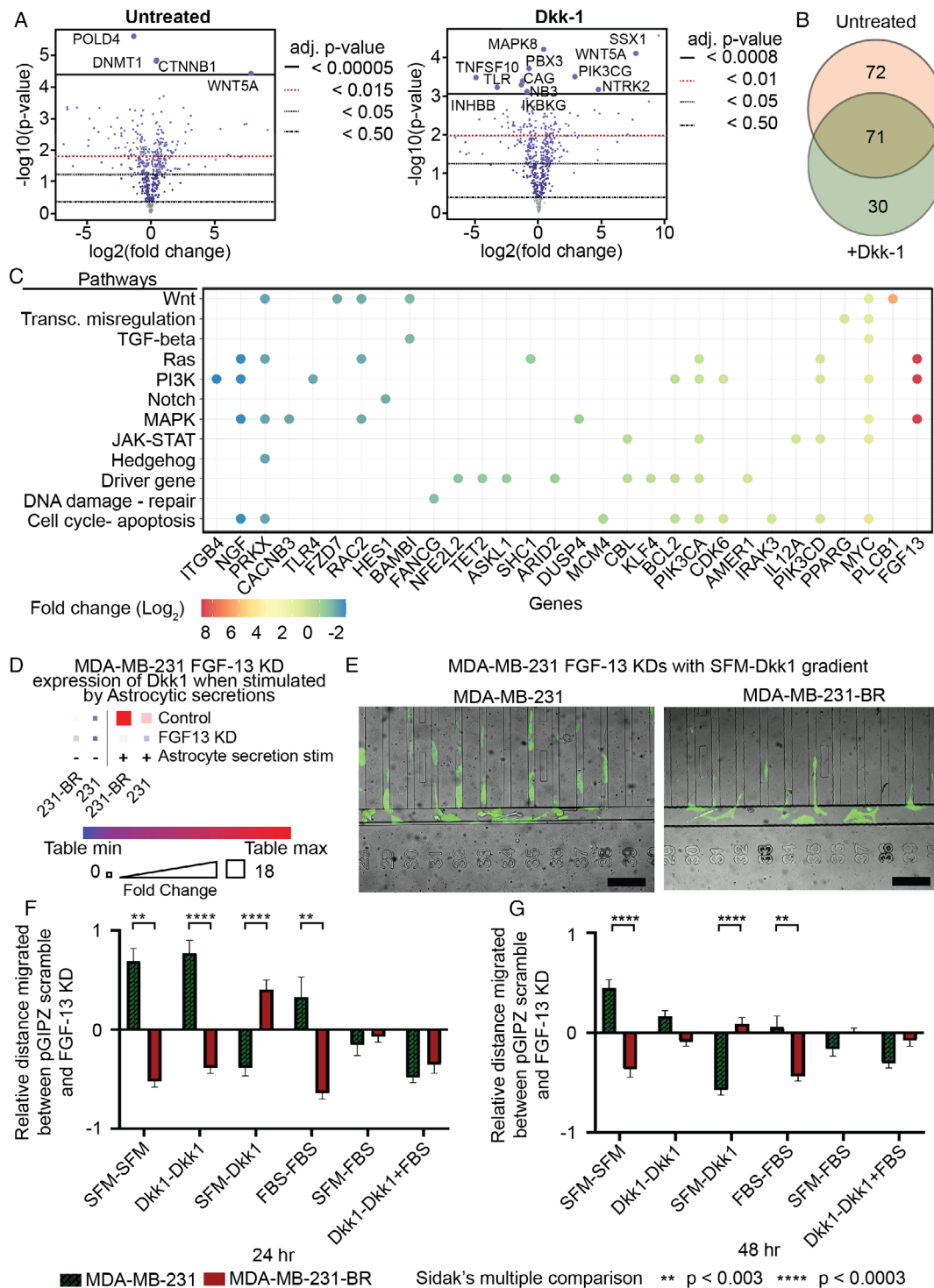


Figure 7. The role of astrocytic Dkk-1 can be regulated by modulating relevant MDA-MB-231-BR pathways. A–C) NanoString gene expression profiling of untreated and Dkk-1 treated MDA-MB-231-BR and MDA-MB-231 cells. (A) Volcano plots of fold change between cell types untreated and treated with Dkk-1 with adjusted p -values. (B) Venn diagram of significant differentially expressed genes, false discovery rate threshold $p < 0.05$. (C) Fold change of significant differentially expressed genes under Dkk-1 stimulation categorized by signaling pathway. (D) ELISA showing Dkk1 found in the secretions of astrocyte-stimulated MDA-MB-231 FGF13 KD and MDA-MB-231-BR FGF13 KD is lowered when FGF13 is KD. (E) Images of MDA-MB-231-BR and MDA-MB-231 cells migrating toward Dkk-1. Scale bars = 200 μm . (F, G) Percent change in distance migrated between FGF-13 knockdown and pGIPZ scramble in Dkk-1 gradients for MDA-MB-231-BR and MDA-MB-231 at (E) 24 h and (F) 48 h. ** $p < 3.0 \times 10^{-3}$, **** $p < 3.0 \times 10^{-4}$ t -tests with Holm–Sidak multiple comparisons test. (A–D) was performed with triplicate technical replicates. (E–G) was performed with three biological replicates each with three technical replicates.

regulating tight junctions within the BBB and may regulate the entire brain microenvironment. Zhang et al. summarized these results showing multiple immunosuppressive effects such as paralyzing T cell migration, mediating proinflammatory molecules such as CD4, and CD8 + T cells activation.^[24] In addition, Heiland et al. found that astrocytes may play a role in suppressing the immune system surrounding glioblastoma, in part by inducing T cell exhaustion through expression of PD-L1. Beyond protein secretions, astrocyte secretion of microRNAs has been shown to induce microenvironment PTEN loss, an important tumor suppressor.^[25]

Moreover, cancer cells may interact with astrocytes by either direct cell–cell interaction or via secretions. Several authors suggest that astrocytes may promote tumor formation by secretions. Liu et al. showed that astrocytes promote medulloblastoma progression through hedgehog secretion.^[26] Another possibility is that astrocytes secrete chemokines that promote extravasation. One example is the CCL2–CCR2 astrocyte–cancer cell receptor interaction found by Hajal et al. that demonstrated CCR2-deficient cancer cells exhibit significantly reduced extravasation in murine models. Neurotrophic factors secreted by astrocytes including TGF- α and CXCL12 may increase invasiveness of GBM cells. These examples indicate that the brain microenvironment is a complex set of interactions between all cells and system that result in promoting certain brain metastasis.

In this study, we utilized the BBN to unravel the physical and secretory interactions between cancer cells and the brain niche cells (endothelial, astrocyte, and microglia). Our previous work has shown that there is differential behavior of the parental MDA-MB-231 and MDA-MB-231-BR cells in the niche that mimics known *in vivo* invasive behavior.^[16] The MDA-MB-231-BR cells would degrade the endothelial barrier at a faster rate than the parental cells and grow more rapidly.^[16,27] In addition here, we found that the cooperative interaction between the cancer and brain niche cells induced remodeling of the BBN. Although this behavior was consistent, the way it was achieved differed according to which cell (cancer or astrocyte) moved the most relative to the endothelial barrier. This behavior suggests that the mechanisms driving these two remodeling schemes may differ. Because this behavior indicates that the cancer cells and astrocytes interact, an important question was if extravasation was driven by physical or chemical signals. Our data support the notion that both physical interaction with astrocytes and their cytokines are important to drive cancer progression in the brain. The data show that this occurs both as a migratory and invasive phenotype. Importantly, MDA-MB-231 brain tropic cells were primarily affected by astrocytes secretions and microglia secretions. However, the strongest effect was observed when the secretions were used to directly stimulate cells. This suggests that the cells require a certain level of cytokine stimulation, before being activated to migrate. Combined with our observation that brain tropic cells degrade the endothelial barrier at a greater rate may form a compelling argument for how these cells develop into more aggressive metastasis. It may be that brain tropic metastases degrade the endothelial layer and are then stimulated by released brain cytokines that draw the cancer cells and astrocytes toward one another.

In the BBN, cancer cells became more spherical when cultured with brain niche cell secretions. This may indicate,

as previously reported, the migratory mechanism being utilized by cells that extravasate deeply into the device. In contrast, the clusters of cells (>10 cells by volume) become flatter, likely as they grow along the endothelial barrier for support. The fact that clusters stay closer to the endothelial barrier than individual cells also indicates that they may be driven by growth, supported by nearby cancer cells. This belies the idea that a single cell may rapidly extravasate and travel some distance before forming a deadly cluster. This observation may be of importance for therapeutics. First, it indicates that clusters of cells form near the BBB. Treatments targeting those cell clusters may leave single cells deeper in the brain niche space that then can proliferate. Second, our data indicates brain tropic cells degrade the BBB during the growth stage. Therefore, cancer cells may form a secondary barrier that reduces drug penetrations into the tumor. From our work, a model emerges in which major changes occur with only the modulation of secretions, so we pose that the barrier must be damaged prior to large-scale invasion of cancer cells and clusters.

A compelling therapeutic target then is to disrupt crosstalk between cancer cells and brain niche cells that drive brain metastasis.^[28] For example, the canonical Wnt-beta catenin pathway is known to control cell proliferation, migration, differentiation, and is critical for mediating astrocyte–neuronal crosstalk in the brain by regulating glutamate uptake for astrocytes.^[29] Wnt signaling is more active in metastatic triple-negative breast cancer (TNBC) compared to nonbasal subtypes of breast cancer and correlates with poor prognoses.^[30] Yet it is unknown which pathway may be therapeutically targeted. This challenge motivated this study to identify secretion-dependent cancer–astrocyte and cancer–microglia interactions. We observed using dual-independent techniques; only Dkk-1 increased when brain niche cells were stimulated with both cancer cells and cancer cell secretions. Dkk-1 is a known modulator of the Wnt-signaling pathway, where increased levels of Dkk-1 can block Wnt-signaling of β -catenin, eventually reducing GS production and glutamine and glutamate metabolism.^[20] Reducing Dkk-1 levels near invading tumor cells may increase metabolite production reducing extravasation.

Astrocytic Dkk-1 influences cancer cell migration and extravasation into the brain niche, as shown by both the migratory behavior of MDA-MB-231 cancer cells when stimulated with Dkk-1 and the significant change in the distance between cancer cells and astrocytes when the BBN is treated with Dkk-1-neutralizing antibody. The mean distance between cancer and astrocyte cells more than doubles because of neutralizing Dkk-1. This is a remarkable change that may highlight a strategy toward preventing the development of a premetastatic niche.

NMR analysis of extracellular MDA-MB-231-BR metabolites revealed an increase in glutamate metabolism, indicating the brain-tropic cell line's inherent metabolic plasticity under brain niche secretion stimulation. Moreover, stimulation with endothelial secretions also increases glutamate metabolism of both MDA-MB-231-BR and MDA-MB-231 cancer cells. Knowing these pathways are enriched and critical to the role of Dkk-1 in the Wnt signaling pathway, we finally observed if cancer gene expression signatures differed under Dkk-1 stimulation. By shRNA knock down of salient Wnt-related genes (FGF-13) that increased in gene expression with Dkk-1 stimulation, we found that cancer

cell migration patterns were altered in the migration chip analysis in Dkk-1 gradients. Specifically, the MDA-MB-231-BR FGF-13 knockdown was less migratory both under direct stimulation and under chemotaxis. The MDA-MB-231 FGF-13 knockdown initially showed mixed migratory behavior but after 48 h, it also exhibited dampened migration in the presence of Dkk-1. However, one concern is that the cells became more migratory under nominal conditions without serum. This could indicate that knocking down FGF-13 may make metabolically restricted cells more migratory.

Several limitations of our study require careful consideration. Exosomal crosstalk, including miRNA modulation, was not evaluated. Moreover, metabolites were not separated from protein secretions, possibly confounding some of the results. Astrocytes and microglia were assessed separately but not cooperatively, and no pericytes were present in our brain niche model. Secretions from stimulated cells also contained the stimulating secretions. This limits the physiological relevance compared to a human model and would be an important next study.

4. Conclusion

In conclusion, using the BBN and migration device, we have highlighted one of the communication strategies that leads to remodeling of the brain niche in premetastatic states in the presence of brain tropic cancer cells. We have also identified key cytokines driving that remodeling process. Finally, we highlighted important changes to the metabolism and upregulated pathways utilized by cancer cells to induce extravasation and remodeling including key regulatory genes.

5. Experimental Section

Cell Culture and Reagents: TNBC MDA-MB-231, the BR-derived line MDA-MB-231-BR-GFP, Her2+ breast cancer JIMT-1, and the BR-derived line JIMT-1-BR cells were obtained from Dr. Patricia Steeg. MDA-MB-231 and JIMT-1 lines were maintained in DMEM supplemented with 4.5 g L⁻¹ glucose, 10% FBS, 2 mM L-glutamine, and 1X antibiotic-antimycotic. Normal human astrocytes (Lonza, CC-3186) were maintained in DMEM supplemented with 4.5 g L⁻¹ glucose, 10% FBS, 2 mM glutamax, 2 mM sodium pyruvate, 1X N2 growth supplement, and 1X antibiotic-antimycotic. Human microglia line HMC3 (ATCC, CRL-3304) were maintained in EMEM supplemented with 10% FBS, 2 mM L-glutamine, 2 mM sodium pyruvate, 1X non-essential amino acids, and 1X antibiotic-antimycotic. Brain microvascular endothelial cell line hCMEC/D3 (Millipore, SCC066) were maintained in endothelial cell growth medium 2 (PromoCell) with 1X antibiotic-antimycotic. All cells in routine cell culture and within microfluidic devices were grown at 37 °C in 5% CO₂. MDA-MB-231, JIMT1, and JIMT1-BR with stable cytoplasmic GFP expression were generated by lentiviral transduction of pLL. EV-GFP empty vector, astrocytes were transduced with pLL3.7-small ultrared fluorescent protein (smURFP), and microglia were transiently stained with efluor proliferation dye 450 according to the manufacturer's instruction. All nonfluorescent cells in each stable fluorescent cell lines were removed using fluorescence-activated cell sorting prior to experimentation (Moflo Astrios cell sorter). For shRNA knockdown studies, pGIPZ-FGF-13 (Dharmacon clone 367 913, 409 644) and pGIPZ scrambled (Dharmacon catalog number RHS4346) were individually transduced into MDA-MB-231 and MDA-MB-231-BR cells.

Assessment of Cancer Cell Extravasation Using a Microfluidic BBN Device: A total of four BBN channels per single chip were used for replicates. The

bottom chamber of each blood brain niche channel was formed with a collagen solution (3 mg mL⁻¹, PureCol) in 1X MEM supplemented with 4.5 g L⁻¹ glucose and sodium bicarbonate and allowed to gel beneath a polycarbonate membrane (5 μm pore size) separating the bottom and top chambers at 37 °C. This collagen mixture was infused with either 1) 125 000 astrocytes stably labeled to express cytoplasmic pLL3.7-smURFP (astrocyte-smURFP), 2) or 18 750 microglia cells stained with eFluor 450 proliferation dye according to the manufacturers protocol (microglia-eF450), or 3) left as a collagen media mixture. Once the bottom chamber was solidified, Matrigel solution (2%, growth factor reduced with phenol red) diluted in endothelial cell complete media coated the top flow channel with the bottom lining membrane containing the brain niche. Brain microvascular endothelial cells stably labeled to express cytoplasmic dsRed (hCMEC/D3-dsRed) were then seeded and form a barrier on the matrigel-coated membrane after 2 days of culture with media exchanged twice daily. Devices containing astrocytes in the brain niche were cultivated using a 50/50 mixture of complete astrocyte and endothelial media. Devices containing microglia in the brain niche were cultured using a 75/25 mixture of complete endothelial/microglia media. μBBN chips were cultured for 2 days to permit BBB formation prior to the addition of cancer cells. All μBBN chips containing no astrocyte or microglia cells were exchanged to contain astrocyte or microglia secretions at 1X concentration in the brain niche. μBBN chips containing astrocyte cells were treated with 10 μg mL⁻¹ Dkk-1 neutralization antibody (R&D systems) in the bottom brain niche side of the chip twice daily. A total of 30 000 cancer cells stably expressing cytoplasmic GFP (pEV-GFP) in single-cell suspension were seeded into each top flow chamber of a μBBN chip and cultured for up to 9 days postseeding to visualize micrometastasis. All BBN chips containing astrocyte-smURFP cells were stimulated with 10 μM biliverdin diluted in the chip media as a cofactor to visualize smURFP fluorescence 24 h prior to imaging each time point.

BBNiche chips were imaged 2 and 9 days after seeding cancer cells using a Nikon A1r fluorescent confocal microscope. Each channel was captured using an XY-tiled z-stack. A previously reported confocal tomography technique was applied for analysis of cancer cell extravasation into the chip and modified to include monitoring of the BBNiche astrocyte and microglia cell positions at each timepoint.^[16,27] This approach extracts individual cellular volumes from the 3D confocal image and reports various cellular characteristics from them including: 1) cell position relative to the endothelial barrier; 2) sphericity as a metric for cell shape; 3) distances between cancer cells and astrocytes or microglia; and 4) cell counts. These methods were expanded to include cluster analysis and structural analysis of the tumor micro-environment. Cluster analysis was done by filtering out 3D volumes less than ten times the median cell volume. The remaining larger volumes were labeled as clusters or BBN micrometastasis and the metrics were re-calculated. The volumes were also broken up using a body centered cubic crystal lattice overlay sized on the median size of the cell population and the individual cells were annotated and added to the list of total cells. For both cells and clusters, resulting distributions for each metric were analyzed to identify subpopulations of cells within the device. This was done by unbiased identification of subpopulations. First the kernel density estimator (KDE) bandwidth for each distribution was selected by scoring the troughs found between peaks along the KDE. The score was determined to identify troughs between peaks that were possible breaks between subpopulations. The score was established using the following equation.

$$S = \sum_0^t P_t + 2G + \bar{D}_t \quad (1)$$

P_t is the summation of the prominence of each trough, G is the number of subpopulations expected, and \bar{D}_t is the average distance between troughs. This approach minimized the number of subpopulations while maximizing the prominence and spacing. Next a k -means fuzzy clustering was used on each cell to determine the probability it belonged to the list of subpopulations. Finally, boot strapping sampling was used to identify the mean, median, and standard error of each subpopulation. This enables

comparison between subpopulations of cells within each device to subpopulations in other devices. Finally, interaction between the cells the niche was measured in two ways. First, the endothelial layer was found by fitting a planar or curved surface to the endothelial cell centroids in the device. Then the distance of cells or clusters to that barrier was measured. Second, the distances between both the centroid and bounding box edges of individual cells of different types were calculated. We performed a minimum of six biological replicates for each experimental condition, and each measurement included thousands of cells. Statistical significance was determined using a Smirnov–Kolmogorov test and Kruskal–Wallis rank sum test ($p < 0.05$) for distributions and t -test with multiple comparison correction for peaks.

Interpreting 2D Density Remodeling Plots: The goal of these plots is to show how cancer cells and resident brain niche cells collocate over time. The 2D density plots convey the interactions between pairs of cancer cells and brain resident cells at specific locations within the blood brain barrier niche. Figure 1b, 2c and 5c shows the legend for interpreting the graph. Darker colors indicate more pairs of cells interacting at a specific location, while lighter colors indicate fewer pairs. These plots are divided into four quadrants that describe where in the BBN device the cells are located. Quadrant 1 shows that the cancer cell in a pair is on the brain side of the device and the astrocyte is on the flow chamber side. Quadrant 2 shows cancer and astrocyte cells are both on the brain side of the device. Quadrant 3 shows both cancer and astrocyte cells on the flow chamber side of the device. Finally, quadrant 4 shows cancer cells in the flow chamber and astrocyte cells in the brain side of the device. The proximity of the cells to each other can be visualized by the distance the pair is from the short, dotted diagonal line. When the two cells touch, they will be plotted on the diagonal line and the further apart they get from each other, the further from the diagonal line they will be. The red overlays in quadrants 1 & 2 show when cancer cells are in the lower 50% of the brain chamber. The blue overlays in quadrants 2 & 4 show when the astrocyte cells are in the lower 50% of the brain chamber. The endothelial barrier is represented by the long-dashed lines. The “distance extravasated” axis indicates the distance (μm) between the cancer cells and the endothelial barrier. Distances ranging from -200 to $0 \mu\text{m}$ are cells that have remained in the microfluidic flow chamber space and have not extravasated through the endothelial barrier. A distance of $-200 \mu\text{m}$ indicates cancer cells that reside in the top of the flow chamber, farthest away from the endothelial barrier positioned at $0 \mu\text{m}$. Positive extravasated distances (greater than $0 \mu\text{m}$) represent cells that have migrated into the brain niche compartment. Cells can maximally travel a distance of $300 \mu\text{m}$ in the brain niche compartment before reaching the bottom of the brain niche chip. While the “distance to the barrier” axis indicates the distance (μm) between the astrocyte cells and the BBB, astrocyte distance to the barrier ranged from 0 to $300 \mu\text{m}$ within the microfluidic chip brain niche component, with $300 \mu\text{m}$ representing the farthest distance from the endothelial barrier. In this way, you can identify how many pairs of cancer cells and astrocytes cells are a certain distance from each other and the endothelial barrier providing a robust understanding of remodeling in the niche.

Assessment of Cell Migration Using a Microfluidic Migration Device: Briefly, the migration chip is constructed out of polydimethylsiloxane (PDMS) and positions single cells at one of the entrances of 40 migration channels that are $1000 \mu\text{m}$ in length, $20 \mu\text{m}$ wide, and $10 \mu\text{m}$ tall (Figure S2a, Supporting Information). Passive diffusion chemoattractant gradients were established, and cells were monitored microscopically at 0 and 24 h to visualize migration. Cancer cell migration was assessed toward two gradients: 1) an increasing concentration of astrocyte, microglia, or endothelial secretions in SFM to address chemotactic qualities of the brain niche secretions; and 2) with each brain niche cell secretion in SFM provided as a stimulus to the cancer cells throughout the entirety of the migration chip, with 10% FBS as an external chemotactic gradient. Astrocyte and endothelial secretory chemotactic gradients did not affect MDA-MB-231-BR or MDA-MB-231 cells migration when provided as a chemoattractant compared to SFM alone. However, in comparison to SFM alone, a chemotactic gradient of microglia secretions significantly influenced parental MDA-MB-231 migration (Figure S2b, Supporting Information). In fact, MDA-MB-231-BR significantly reduced their migratory capacity in the

presence of microglia secretions compared to SFM only. We then provided the individual brain niche secretions as a potentially stimulatory factor to induce them to migrate toward an external gradient of FBS, to ascertain the ability of the secretions to convert nonmigratory cancer cells toward a migratory phenotype. Astrocyte and endothelial secretions stimulated MDA-MB-231-BR migration toward an FBS gradient compared to baseline migration toward an FBS gradient alone (Figure S2c, Supporting Information). Although microglia secretion gradients were sufficient to promote parental MDA-MB-231 migration, the microglia secretions did not promote parental MDA-MB-231s to increase their migration toward external FBS gradients. Importantly, no statistically significant cell growth was detected over the 24 h migration period in all gradient conditions (Figure S2d–e, Supporting Information).

The migration chips design and utility has been described in previous reports and were built in the same manner out of PDMS with biopsy punches to form the inlets and outlets and bonded to glass slides using an oxygen plasma treatment.^[17,31] Degassed migration chips are coated with collagen I ($1 \mu\text{g mL}^{-1}$) lining of all channels for 18 – 24 h in a tissue culture incubator and then rinsed with HBSS under flow conditions to remove excess collagen.^[27] Single-cell suspensions of cancer cells were seeded into the top-left reservoir and flowed down toward the bottom-left reservoir with the opportunity to attach to the entrances of the horizontal migration channels. Excess, non-attached cells were removed with excess complete media; then the cancer cells were incubated at 37°C , $5\% \text{ CO}_2$ to permit cell adherence for 2 h . The migration chips were washed with HBSS + Ca/Mg under flow and then exchanged into appropriate experimental conditions to form 1) chemoattractant gradients of astrocyte, microglia, and endothelial secretions or 20 ng mL^{-1} -purified human Dkk-1 (Peprotech) in SFM and 2) secretion or 20 ng mL^{-1} Dkk-1 stimulation in SFM with an FBS gradient. Epifluorescent phase contrast images were captured at 0 and 24 h . Using a Python script, cell migration was calculated as the distance (μm) in the horizontal position of the cell to the beginning of the seeding channel to encompass non-migratory cell populations residing at the entrances to the migration channels. Plotted data represent 3–5 separate biological replicates, for an average of 215 cell migration distances per experimental condition (range: 147 – 419 cells). Statistical significance was determined by Mann–Whitney t -test and a Bonferroni correction ($p < 0.00625$).

Secretion Collection: Astrocytes, microglia, and endothelial cells were seeded into dishes at 60% confluence and cultured overnight. Each cell type was either left in basal media or stimulated with MDA-MB-231-BR cells, MDA-MB-231-BR secretions, MDA-MB-231 cells, or MDA-MB-231 secretions the following day. Empty dishes were also seeded with the same components used for stimulation: MDA-MB-231-BR cells, MDA-MB-231-BR secretions, MDA-MB-231 cells, MDA-MB-231 secretions, or basal media and carried as controls. Conditioned media containing cellular secretions were collected after 24 h of interaction with the cancer cells, centrifuged to remove any debris/particulates, and frozen at -80°C until use. Similarly, cancer cells seeded into dishes were left unstimulated or stimulated with astrocyte, microglia, and endothelial cells or paired secretions for collection after 24 h . Again, empty dishes were also seeded with astrocyte, microglia, and endothelial cells or secretions and carried as controls.

Cytokine Profile Identification: Assessment of cytokines secreted by all brain niche and cancer cells was performed using Proteome Profiler Human XL cytokine array (R&D Systems) according to the manufacturer’s protocol using $500 \mu\text{L}$ of each secretion. One biological replicate of each experimental sample was assayed in technical duplicates. All dot blots were exposed to film for 10 s before developing. The dot blot intensities were quantified using Quick Spots Tool (Western Vision Software). Fold change of cytokine expression in stimulated compared to unstimulated controls was calculated and plotted using the Morpheus software (Broad Institute). Statistical significance was determined using multiple t -tests with a Benjamini, Krieger, and Yekutieli false discovery rate correction in Prism.

Cytokine Quantification: Collected secretions were concentrated $10\times$ using Amicon Ultra centrifugal filters with a 3 kDa molecular weight cut off and submitted to the University of Michigan Rogel Cancer

Center Immunology core for ELISA quantification. Assays included: Human Dkk-1 (Quantikine kit, R&D Systems), MCP-1, IL-8, CXCL5, GM-CSF, IL-6, Gro-1, and VEGF. A total of four biological replicates were assayed in technical duplicates. Raw cytokine concentrations of control media used for stimulation were subtracted from each experimental sample accordingly and corrected by total protein content (BCA, ThermoFisher). Resulting cytokine levels were normalized to their paired unstimulated control condition. Heatmaps were plotted using Morpheus software (Broad Institute) and statistical significance was determined using multiple *t*-tests with a Benjamini, Krieger, and Yekutieli false discovery rate correction in Prism.

Extracellular Metabolite Quantification: A single biological replicate for each experimental sample was submitted to the University of Michigan College of Pharmacy NMR core for metabolite quantification. Nanosep centrifugal devices (Pall Corporation) with a 3 Kda molecular weight cut off were prerinsed x3 with ultrapure water and then x1 with deuterated water (Sigma Aldrich). Metabolite samples (500 μ L per sample) were then filtered through the prerinsed devices to remove proteins according to manufacturer's specifications (14 000xg at 4 $^{\circ}$ C for 20 min). After filtration, 50 μ L deuterated water was applied to the top of the filter, vortexed, then centrifuged again to collect all metabolites in the filtrate. 50 μ L of DSS internal standard (IS) was added to each sample; then samples were stored at -80° C in cryovials until the NMR assay was performed. The 1D-1H-NMR spectrum of each filtered cell media sample was acquired on an Agilent, 500 MHz NMR spectrometer with a VNMR5 console operated by host software VNMRJ 4.0 and equipped with a 5 mm One-Probe. The Chenomx internal standard (IS), DSS-d6 (3-(Trimethylsilyl)-1-propanesulfonic acid-d6 sodium salt) was used as a reference signal for the quantification of metabolites. On the day of the NMR experiments, samples were thawed, pH was measured and adjusted to be within 6.5-7.5 range, and 32 scans were collected. The NMR experiment, which consisted of the first increment of a 1H,1H-NOESY (commonly referred to as a 1D-NOESY or METNOESY) pulse sequence, was as follows: a 1 s recovery delay, a 990 ms saturation pulse of 80 Hz (γ B1) -induced field strength empirically centered on the water resonance, two calibrated 90° pulses, a mixing time (tmix) of 100 ms, a final 90° pulse, and an acquisition period of 4 s. Optimal excitation pulse widths were obtained utilizing an array of pulse lengths to determine the 360° pulse null for water and dividing by 4 to obtain the 90° optimum. Spectra were acquired at a room temperature of 298 ± 0.3 K. The resulting NMR spectra were analyzed using Chenomx NMR Suite 8.3 (Chenomx, Inc.). The processor module was used to phase shift and baseline correct each spectrum. Compounds were then identified and quantified in the profiler module of the software, which accounts for the pH of the sample and the concentration of the IS and quantifies metabolite concentration relative to the IS. Metabolite identity was confirmed using the Chenomx Compound Library, which contained >300 compounds. Around 32 compounds resulted in the Chenomx library used on the cell media fluids to identify and quantify metabolites with various degrees of certainties. The differences in metabolite concentrations in conditioned cell culture media from concentrations in the control medium utilized for stimulation were corrected by total protein content (BCA, ThermoFisher). Resulting metabolite concentrations were normalized to their paired unstimulated control condition and analyzed using Metaboanalyst 4.0 software for metabolite pathway enrichment (Xia lab, McGill University). Heatmaps were plotted using the Morpheus software (Broad Institute).

BBN Microfluidic Device Fabrication and Assembly: The BBN design was described in previous reports and were built in the same manner out of PDMS with biopsy punches to form the inlets and outlets.^[16,27] A polycarbonate 5 μ m polymer porous membrane divided the upper and lower chambers on which the endothelial layer was cultured. The μ BBN devices were bonded to 50 mm \times 75 mm glass slides after oxygen plasma treatment (50 W, 30 s). P200 pipette tips were cut and used for media reservoirs in the BBN chip.

NanoString gene Expression Profiling: Six-well plates were seeded with 0.15×10^6 MDA-MB-231-BR or MDA-MB-231 cells/well and allowed to attach overnight and then treated with 20 ng mL⁻¹-purified human Dkk-1 for 24 h or left untreated. RNA isolations were performed using the

Rneasy mini kit (Qiagen) and assessed for quantity and purity using a nanodrop (ThermoFisher). Gene expression was assessed using a NanoString Human PanCancer Pathways codeset according to the manufacturer's instruction and further analyzed using the nCounter Advanced Analysis Module which normalizes gene expression to a set of positive and negative controls and optimizes housekeeping genes using linearity across the dataset. nCounter software was utilized to convert raw gene counts to Log₂ fold changes of MDA-MB-231-BR versus MDA-MB-231 with and without Dkk-1 treatment. Statistically significant *p*-values of differential expression were determined by the nCounter software using *t*-tests and a Benjamini–Hochberg correction, *p* < 0.05. Statistically significant differentially expressed genes that were exclusive to the Dkk-1 treatment were determined and plotted in R and were assorted by signaling pathway as dictated by the NanoString panel.

Statistical Analysis: Statistical analysis was performed using R scripts (μ BBN chip data) and Prism (2D migration, dot blot, ELISA analyses) and Python's Scikit. Comparisons between the populations of cells within μ BBN chips were made using Smirnov–Kolmogorov tests and Kruskal–Wallis rank sum test (*p* < 0.05). Statistical significance of the average cell migration in 2D in the microfluidic migration chips was determined using multiple Mann–Whitney *t*-tests with a Bonferroni correction (*p* < 0.00625). For comparison between subpopulations within a distribution of cell metrics (distance extravasated, sphericity) statistical significance was determined using a *t*-test with multiple comparison correction for peaks.

Comparisons between each chemotactic gradient of BBN secretions and the SFM–SFM control were performed. Stimulatory gradients of secretions were tested for statistical significance by comparing against the SFM–FBS and FBS–FBS controls. Relative changes between FGF-13 knockdowns and pGIPZ scramble controls used Holm–Šidák multiple comparisons test. The mean dot blot intensities and ELISA concentrations of MDA-MB-231-BR and parental MDA-MB-231 secretions under each stimulation condition were determined to be statistically significant using multiple *t*-tests with a Benjamini, Krieger, and Yekutieli false discovery rate correction. Similarly, brain niche cells stimulated with MDA-MB-231-BR or MDA-MB-231 were compared for significance for dot blot and ELISA assays. The values for *n*, *p*, and the specific statistical test performed for each experiment are included in the appropriate figure legend and main text.

Supporting Information

Supporting Information is available from the Wiley Online Library or from the author.

Acknowledgements

The authors would like to thank Dr. Patricia Steeg's Lab, at the National Cancer Institute, for the generous donation of MDA-MB-231-BR-GFP, JIMT1, and JIMT1-BR cells. pLenti-smURFP was a gift from Erik Rodriguez and Roger Tsien (Addgene plasmid #80349; <http://n2t.net/addgene:80349>; RRID:Addgene 80349). The authors thank several University of Michigan Biomedical Research Core Facilities for contributions to this work: The vector core for subcloning and lentiviral preparation, fluorescence-activated cell sorting was performed at the flow cytometry Core, and the microscopy core for confocal microscopy of the blood–brain niche devices. Confocal microscopy was also performed at the University of Michigan Biointerface Institute (BI). The authors wish to thank Joel Whitfield of the University of Michigan Rogel Cancer Center Immunology Core for ELISA analysis, Dr. Larisa Yeomans at the University of Michigan College of Pharmacy NMR core for analysis and quantification of metabolites, Kelley Kidwell and Ryan Ross, University of Michigan School of Public Health, Department of Biostatistics for statistical consultation, and Dr. Abhinav Achreja for helpful suggestions. T.M.W. was partially supported by 1R21CA245597-01 and the National Center for Advancing Translational Sciences of the National Institutes of Health under award number UL1TR002240. C.R.O. was partially supported by NIH T-32 Training Fellowship (T32CA009676) and 1R21CA245597-01.

Funding for materials and characterization was provided by National Cancer Institute of the National Institutes of Health under award numbers 1R21CA245597-01, P3CA046592, 5T32CA009676-23, CA196018, AI116482, METAvivor Foundation, and the Breast Cancer Research Foundation. The content is solely the responsibility of the authors and does not necessarily represent the official views of the National Institutes of Health.

Conflict of Interest

The authors declare no conflict of interest.

Author Contributions

T.M.W. and S.D.M. conceived the study. T.M.W. performed all experiments for this study. M.A., C.R.O., N.M., L.R., A.M., and J.A.Y. assisted T.M.W. with experiments. T.M.W., C.R.O., P.U., B.Y., and S.D.M. analyzed the data and performed statistical significance tests. C.R.O. wrote the software used for analysis. C.R.O., A.M., M.G., and S.D.M. analyzed results for data interpretation. The original manuscript and figure plan were drafted by T.M.W. All authors participated in the review and final editing of this manuscript.

Data Availability Statement

The data that support the findings of this study are openly available in [Zenodo] at [10.5281/zenodo.6376563], reference number [6376563].

Keywords

blood–brain barrier, cancer, dkk-1, metastasis, microenvironments, microfluidic, secretome

Received: April 1, 2022

Revised: December 14, 2022

Published online:

- [1] a) D. N. Cagney, A. M. Martin, P. J. Catalano, A. J. Redig, N. U. Lin, E. Q. Lee, P. Y. Wen, I. F. Dunn, W. L. Bi, S. E. Weiss, D. A. Haas-Kogan, B. M. Alexander, A. A. Aizer, *Neuro-Oncology* **2017**, *19*, 1511; b) J. Jin, Y. Gao, J. Zhang, L. Wang, B. Wang, J. Cao, Z. Shao, Z. Wang, *BMC Cancer* **2018**, *18*, 446.
- [2] a) C. L. Ihle, M. D. Provera, D. M. Straign, E. E. Smith, S. M. Edgerton, A. Van Bokhoven, M. S. Lucia, P. Owens, *J. ImmunoTher. Cancer* **2019**, *7*, 293; b) Y. I. Deng, E. Verron, R. Rohanzadeh, *Anticancer Res.* **2016**, *36*, 5639.
- [3] U. H. Weidle, J. Niewohner, G. Tiefenthaler, *Cancer Genomics Proteomics* **2015**, *12*, 167.
- [4] A. S. Achrol, R. C. Rennert, C. Anders, R. Soffietti, M. S. Ahluwalia, L. Nayak, S. Peters, N. D. Arvold, G. R. Harsh, P. S. Steeg, S. D. Chang, *Nat. Rev. Dis. Primers* **2019**, *5*, 5.
- [5] M. Lorger, B. Felding-Habermann, *Am. J. Pathol.* **2010**, *176*, 2958.
- [6] D. Wasilewski, N. Priego, C. Fustero-Torre, M. Valiente, *Front. Oncol.* **2017**, *7*, 298.
- [7] S. A. Liddel, B. A. Barres, *Immunity* **2017**, *46*, 957.
- [8] N. Priego, L. Zhu, C. Monteiro, M. Mulders, D. Wasilewski, W. Bindeman, L. Doglio, L. Martinez, E. Martinez-Saez, Y. C. S. Ramon, D. Megias, E. Hernandez-Encinas, C. Blanco-Aparicio, L. Martinez, E. Zarzuela, J. Munoz, C. Fustero-Torre, E. Pineiro-Yanez, A. Hernandez-Lain, L. Bertero, V. Poli, M. Sanchez-Martinez, J. A. Menendez, R. Soffietti, J. Bosch-Barrera, M. Valiente, *Nat. Med.* **2018**, *24*, 1024.
- [9] P. S. Steeg, *Nat. Rev. Clin. Oncol.* **2021**, *18*, 696.
- [10] M. Valiente, A. C. Obenauf, X. Jin, Q. Chen, X. H. Zhang, D. J. Lee, J. E. Chaff, M. G. Kris, J. T. Huse, E. Brogi, J. Massague, *Cell* **2014**, *156*, 1002.
- [11] B. Gril, A. N. Paranjape, S. Woditschka, E. Hua, E. L. Dolan, J. Hanson, X. Wu, W. Kloc, E. Izycka-Swieszezowska, R. Duchnowska, R. Peksa, W. Biernat, J. Jassem, N. Nayyar, P. K. Brastianos, O. M. Hall, C. J. Peer, W. D. Figg, G. T. Pauly, C. Robinson, S. Diflippantonio, E. Bialecki, P. Metellus, J. P. Schneider, P. S. Steeg, *Nat. Commun.* **2018**, *9*, 2705.
- [12] M. S. Soto, N. R. Sibson, *Front. Cell Neurosci.* **2018**, *12*, 414.
- [13] S. Y. Wu, K. Watabe, *Front. Biosci.* **2017**, *22*, 1805.
- [14] H. You, S. Baluszek, B. Kaminska, *Front. Immunol.* **2019**, *10*, 1941.
- [15] a) M. D. Dun, R. J. Chalkley, S. Faulkner, S. Keene, K. A. Avery-Kiejda, R. J. Scott, L. G. Falkenby, M. J. Cairns, M. R. Larsen, R. A. Bradshaw, H. Hondermarck, *Mol. Cell Proteomics* **2015**, *14*, 2316; b) M. Tanner, A. I. Kapanen, T. Junntila, O. Raheem, S. Grenman, J. Elo, K. Elenius, J. Isola, *Mol. Cancer Ther.* **2004**, *3*, 1585.
- [16] C. R. Oliver, M. A. Altemus, T. M. Westerhof, H. Cheriyan, X. Cheng, M. Dziubinski, Z. Wu, J. Yates, A. Morikawa, J. Heth, M. G. Castro, B. M. Leung, S. Takayama, S. D. Merajver, *Lab Chip* **2019**, *19*, 1162.
- [17] S. G. Allen, Y. C. Chen, J. M. Madden, C. L. Fournier, M. A. Altemus, A. B. Hiziroglu, Y. H. Cheng, Z. F. Wu, L. Bao, J. A. Yates, E. Yoon, S. D. Merajver, *Sci. Rep.* **2016**, *6*, 39190.
- [18] a) M. Lanza, G. Casili, M. Campolo, I. Paterniti, C. Colarossi, M. Mare, R. Giuffrida, M. Caffo, E. Esposito, S. Cuzzocrea, *Brain Sci.* **2021**, *11*, 466; b) D. Matias, J. Balça-Silva, G. C. da Graça, C. M. Wanjiru, L. W. Macharia, C. P. Nascimento, N. R. Roque, J. M. Coelho-Aguiar, C. M. Pereira, M. F. Dos Santos, L. S. Pessoa, F. R. S. Lima, A. Schanaider, V. P. Ferrer, V. Moura-Neto, S. Tania Cristina Leite de Sampaio e Spohr, *Front. Cell. Neurosci.* **2018**, *12*, 235; c) E. D. Osipova, O. V. Semyachkina-Glushkovskaya, A. V. Morgun, N. V. Pisareva, N. A. Malinovskaya, E. B. Boitsova, E. A. Pozhilenkova, O. A. Belova, V. V. Salmin, T. E. Taranushenko, M. Noda, A. B. Salmina, *Rev. Neurosci.* **2018**, *29*, 567.
- [19] S. Malladi, D. G. Macalinao, X. Jin, L. He, H. Basnet, Y. Zou, E. de Stanchina, J. Massague, *Cell* **2016**, *165*, 45.
- [20] Y. C. Shao, Y. Wei, J. F. Liu, X. Y. Xu, *Am. J. Cancer Res.* **2017**, *7*, 1754.
- [21] E. O'Brien, C. Howarth, N. Sibson, *Front. Cell. Neurosci.* **2013**, *7*, 40.
- [22] a) S. Tiwary, J. E. Morales, S. C. Kwiatkowski, F. F. Lang, G. Rao, J. H. McCarty, *Sci. Rep.* **2018**, *8*, 8267; b) J. K. Wrobel, M. Toborek, *Mol. Med.* **2016**, *22*, 32.
- [23] H. Zhang, Y. Zhou, B. Cui, Z. Liu, H. Shen, *Biomed. Pharmacother.* **2020**, *126*, 110086.
- [24] a) N. Priego, M. Valiente, *Front. Immunol.* **2019**, *10*, 1314; b) D. Henrik Heiland, V. M. Ravi, S. P. Behringer, J. H. Frenking, J. Wurm, K. Joseph, N. W. C. Garrelfs, J. Strähle, S. Heynckes, J. Grauvogel, P. Franco, I. Mader, M. Schneider, A.-L. Potthoff, D. Delev, U. G. Hofmann, C. Fung, J. Beck, R. Sankowski, M. Prinz, O. Schnell, *Nat. Commun.* **2019**, *10*, 2541.
- [25] L. Zhang, S. Zhang, J. Yao, F. J. Lowery, Q. Zhang, W.-C. Huang, P. Li, M. Li, X. Wang, C. Zhang, H. Wang, K. Ellis, M. Cheerathodi, J. H. McCarty, D. Palmieri, J. Saunus, S. Lakhani, S. Huang, A. A. Sahin, K. D. Aldape, P. S. Steeg, D. Yu, *Nature* **2015**, *527*, 100.
- [26] Y. Liu, L. W. Yuelling, Y. Wang, F. Du, R. E. Gordon, J. A. O'Brien, J. M. Y. Ng, S. Robins, E. H. Lee, H. Liu, T. Curran, Z.-J. Yang, *Cancer Res.* **2017**, *77*, 6692.
- [27] C. R. Oliver, T. M. Westerhof, M. G. Castro, S. D. Merajver, *J. Visualized Exp.* **2020**, *162*, e61654.
- [28] a) W. Dai, H. Zhu, G. Chen, H. Gu, Y. Gu, X. Sun, X. Zeng, *J. Thorac. Dis.* **2016**, *8*, E1450; b) I. Martínez-Reyes, N. S. Chandel, *Nat. Rev. Cancer* **2021**, *21*, 669.

- [29] V. Lutgen, S. D. Narasipura, A. Sharma, S. Min, L. Al-Harhi, *J. Neuroinflammation* **2016**, *13*, 242.
- [30] F. Klemm, A. Bleckmann, L. Siam, H. N. Chuang, E. Rietkotter, D. Behme, M. Schulz, M. Schaffrinski, S. Schindler, L. Trumper, F. Kramer, T. Beissbarth, C. Stadelmann, C. Binder, T. Pukrop, *Carcinogenesis* **2011**, *32*, 434.
- [31] Y. C. Chen, S. G. Allen, P. N. Ingram, R. Buckanovich, S. D. Merajver, E. Yoon, *Sci. Rep.* **2015**, *5*, 9980.